Polarization Conversion and OAM Generation with a Single Transmitting Metasurface

Zhong Yu, Li Shi*, and Zhenghui Xin

Abstract—We propose a transmitting metasurface (TMS) with ultra-high polarization conversion properties and carrying orbital angular momentum (OAM) vortex waves based on Ku-band's unique periodic unit cell structure. The TMS periodic unit cell structure consists of four cascaded metal layers with parallel-stripe double-arrow and three dielectric layers. We theoretically explain the ultra-high polarization conversion properties of the periodic unit cell by introducing the Jones matrix. Meanwhile, the transmission loss of the periodic unit cell is less than $2.92\,\text{dB}$, and a phase shift of 2π is obtained in 17–19 GHz. We design OAM modes of ± 1, ± 2, and ± 3 for 2π full-phase controlled TMSs by combining the multilayer cascade structure with the Pancharatnam-Berry (P-B) phase principle. The processed TMS produced a vortex wave with an OAM mode of $+2$ and achieved a polarization conversion rate (PCR) of 83.3% under left-hand circular polarization (LHCP) to right-hand circular polarization (RHCP) in agreement with the simulated and measured data. The results show that vortex waves also have the advantages of high efficiency, broadband, and high mode purity. The generated vortex waves are available for fast beam alignment, which is significant for unmanned aerial vehicles (UAVs) and satellite communications in the Ku band.

1. INTRODUCTION

Vortex electromagnetic waves carrying orbital angular momentum (OAM) can expand channel capacity and improve spectral efficiency in wireless communications due to inter-modal orthogonality and theoretical infinity. Since long-range transmission and multiplexing of OAM waves remain controversial [1, 2], they are also widely applied in other fields, such as target detection [3], enhancing the performance of radar systems [4], and manipulating antenna systems [5]. It is worth noting that basically all applications of OAM waves depend on the alignment of the beam axis and initial phase. OAM assists in the alignment of spatial light modulators (SLMs) in the optical domain [6] due to the azimuthal phase factor $\exp(il\varphi)$ carried by OAM with phase singularity and vortex properties. Nevertheless, there are few research reports on using OAM for alignment in the Ku-band since the first introduction of OAM in the RF band by Tamburini et al. [7]. Ku-band is widely applied to unmanned aerial vehicles (UAVs) [8, 9] and satellite communications [10, 11] due to the advantages of broad bandwidth, small flap width, and high positioning accuracy. The methods of generating Ku-band OAM waves include spiral phase plate (SPP) [12], uniform circular array (UCA) [13], metasurface (MS) [14], and transmitarrays (TAs) [15].

TMS has emerged as an up-and-coming contender for OAM antennas due to its low cost, simple feeding, and easy alignment. Previous researchers have proposed many periodic unit cells structures for TAs and transmitting metasurface (TMS), such as C-shaped resonant rings (CSRRs) [16, 17], nested semi-circles [18, 19], extended microstrip patches [20], Jerusalem crosses [21], and arrow structures [22]. The TMS consists of a double-layer arrow [22] with 54% and 39% transmission efficiencies in $l = 1$

and $l = 2$ modes, respectively. The double-layered arrows with a single dielectric layer bring strong dispersion, which deteriorates the operating bandwidth [22]. Three CSRRs and square metal rings cascaded [16] with the TMS can obtain 2-bit coded OAM waves at 14.2–15.2 GHz. A cascade structure of rectangular metal rods with TMS is introduced on the unit cells structure of [16, 17], and the vortex wave is realized with 2-bit phase and 1-bit amplitude coding at 14.35–14.95 GHz (FBW = 4.09%). The dimension expansion method of single-layer TMS [20] produces OAM waves with $l = 1, 2, 4$ at 18 GHz. TMSs are challenging to achieve high polarization conversion rate (PCR) and broad bandwidth based on cellular structures, and often multilayer structures need to be introduced. Meanwhile, the transmission efficiency of single-layer TMS has been shown theoretically to be no more than 25% [23, 24]. Therefore, it is necessary to propose a TMS composed of multilayer periodic unit cells, which can efficiently and stably generate Ku-band broadband OAM waves to assist the alignment of UAVs and satellite beams.

This letter proposes a periodic unit cell structure with parallel-stripe double-arrow, combined with Pancharatnam-Berry (P-B) phase in Ku-band to design OAM mode ± 1, ± 2, ± 3 polarization conversion TMSs. The proposed TMS has a nearly perfect PCR for interconversion of left-handed circular polarization (LHCP) and right-handed circular polarization (RHCP). Experimental measurements verified the performance of vortex wave generation on the TMS, with the analysis and calculation of OAM purity and efficiency. The structure of the letter is as follows. Section 2 is the periodic unit cell's theoretical analysis and performance demonstration. Section 3 shows the analysis of the proposed TMS simulation and measurement data. Section 4 is the conclusion.

2. THEORETICAL ANALYSIS & UNIT CELL DESIGN

2.1. Scattering Field Construction

The reflected and transmitted waves are generated on the scatterer when the incident wave irradiates the scatterer for the periodic unit cell scatterer in Fig. 1. Since this paper focuses on TMS, reflected waves are not analyzed. We denote the field distribution of the incident wave generation as $\mathbf{E_{inc}}$ and the field distribution of the transmitted wave as $\mathbf{E_{out}}$.

$\mathbf{E_{inc}}$ and $\mathbf{E_{out}}$ can be decomposed into two mutually orthogonal components E_{ix} (E_{iy}) and $E_{ty}(E_{ty})$ along the X- (Y-)direction, while the Jones matrix $\mathbf{J}$ is introduced to relate the transmitted wave to
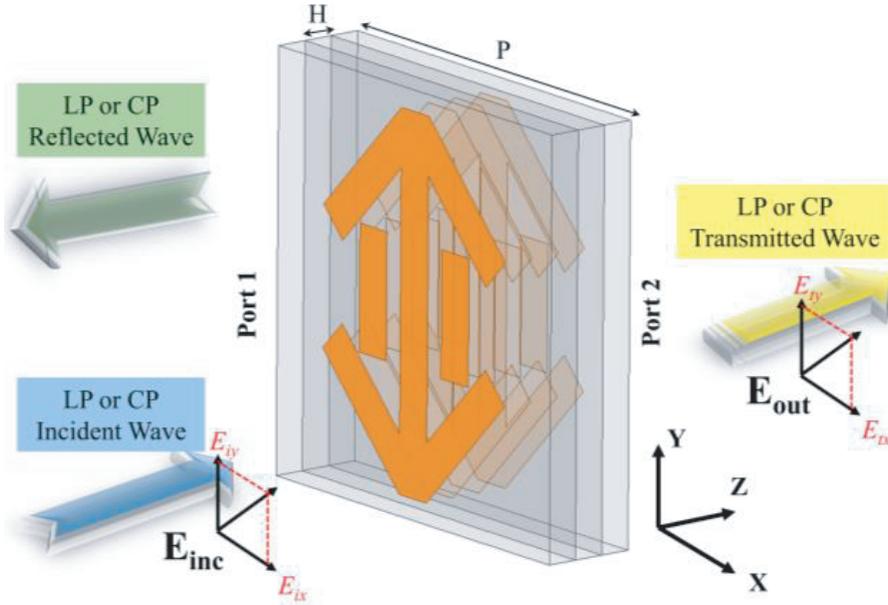

Figure 1. Scattering field description diagram.

the incident wave:

$$\begin{pmatrix} E_{tx} \\ E_{ty} \end{pmatrix} = \mathbf{J} \cdot \mathbf{E_{inc}} = \begin{pmatrix} J_{xx} & J_{xy} \\ J_{yx} & J_{yy} \end{pmatrix} \cdot \begin{pmatrix} E_{ix} \\ E_{iy} \end{pmatrix} \tag{1}$$

where J_{xx} and J_{yy} are co-polarization terms, and J_{xy} and J_{yx} are cross-polarization terms. For example, J_{xy} denotes the transmission coefficient of a line polarization (LP) wave incident along the Y-direction and an LP wave out along the X-direction. If the center of the unit cell rotates the scatterer, the new transmission matrix $\mathbf{J_{rot}}$ can be obtained after the rotation:

$$\mathbf{J_{rot}} = \begin{pmatrix} \cos(\varphi_r) & \sin(\varphi_r) \\ -\sin(\varphi_r) & \cos(\varphi_r) \end{pmatrix}^{-1} \mathbf{J} \begin{pmatrix} \cos(\varphi_r) & \sin(\varphi_r) \\ -\sin(\varphi_r) & \cos(\varphi_r) \end{pmatrix} \tag{2}$$

$$\mathbf{E_{out}} = \mathbf{J_{rot}} \cdot \mathbf{E_{inc}} \tag{3}$$

where φ_r is the counterclockwise rotation angle of the periodic unit cell by its center. Considering the case of circularly polarized (CP) wave incidence, we convert the Cartesian basis to a circularly polarized basis by transforming the matrix Λ [25]. From this, the transmission field of the scatterer is deduced as follows:

$$\begin{pmatrix} E_{LH}^{out} \\ E_{RH}^{out} \end{pmatrix} = \mathbf{\Lambda^{-1}} \mathbf{J_{rot}} \mathbf{\Lambda} \begin{pmatrix} E_{LH}^{inc} \\ E_{RH}^{inc} \end{pmatrix} = \mathbf{J_{circ}^{rot}} \cdot \mathbf{E_{inc}} \tag{4}$$

With

$$\mathbf{\Lambda} = \frac{1}{\sqrt{2}} \begin{pmatrix} 1 & 1 \\ i & -i \end{pmatrix} \tag{5}$$

where $E_{LH}^{out}(E_{RH}^{out})$ denotes the LHCP (RHCP) component in the transmitted wave, and E_{LH}^{inc} (E_{RH}^{inc}) denotes the LHCP (RHCP) component in the incident wave. Assuming that $J_{xy} = J_{yx} = 0$, we can further derive the transmission matrix $\mathbf{J_{circ}^{rot}}$ as follows:

$$\mathbf{J_{circ}^{rot}} = \frac{1}{2} \begin{pmatrix} J_{xx} + J_{yy} & (J_{xx} - J_{yy})\, e^{-2i\varphi_r} \\ (J_{xx} - J_{yy})\, e^{2i\varphi_r} & J_{xx} + J_{yy} \end{pmatrix} \tag{6}$$

We introduce $\exp(il\varphi)$ utilizing the spin-to-orbital coupling effect [26]. The spin angular momentum (SAM) can be converted into OAM according to the P-B phase principle and momentum conservation law [27] as the incident beam passes through an anisotropic TMS. Based on the above analysis, the phase factor $\exp(\pm i2\varphi_r)$, which exactly corresponds to the azimuthal phase factor $\exp(il\varphi)$ of the vortex beam, is successfully introduced in Eq. (6), and the rotation angle of the periodic unit cell is designed with $\varphi_r = l\varphi/2$ (l is the expected OAM mode, and φ is the azimuth angle), thus introducing the vortex phase. This establishes the connection between the azimuth angle φ and the rotation angle φ_r of the periodic unit cell, so that the phase control can be realized by the rotation angle of the periodic unit cell, which is in accordance with the Pancharatnam-Berry phase principle.
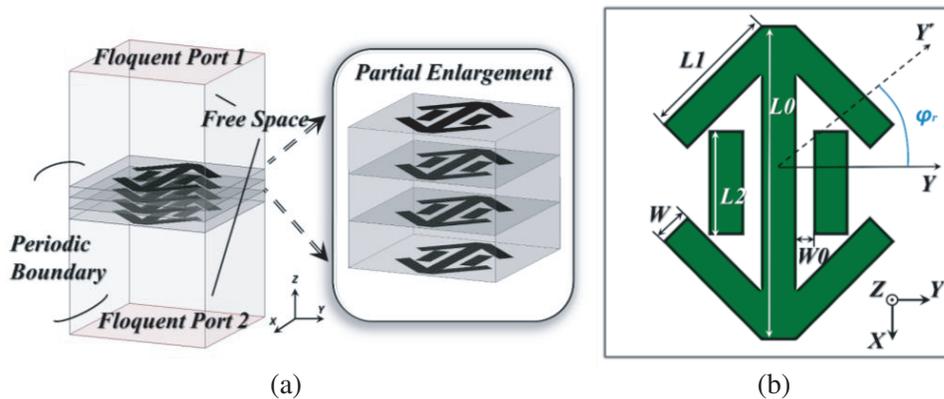

Figure 2. TMS periodic unit cell. (a) 3D structure diagram. (b) Element dimension.

Figure 2 demonstrates the layered structure of the TMS periodic unit cell and the parallel-stripe double-arrow pattern. The periodic unit cell consists of four metal layers and three dielectric layers in Fig. 2(a), which are RO4450B laminates. The dielectric layer is AD255C ($\varepsilon_r = 2.55$, $\tan\delta = 0.0014$), and its dimensions are $8.00 \times 8.00 \times 0.75\,\text{mm}^3$. Additionally, the top and bottom of the periodic unit cell structure create Floquent ports, and the surrounding X-Z plane and Y-Z plane add two periodic master-slave boundary conditions for unit cell simulation of transmission magnitude and phase. Fig. 2(b) presents the metal layer topology of the parallel-stripe double-arrow used to obtain sufficient phase difference. Based on this, a parametric analysis of the metal layer takes place. Table 1 is the optimized specific parameters.

Table 1. Design parameters of the unit cell.

Parameters	Value (mm)	Parameters	Value (mm)
W	1.00	L_1	3.50
W	0.50	L_2	2.80
L	7.00	H	0.75
P	8.00		

2.2. Periodic Unit Cell Performance Analysis

The periodic unit cell simulation results are obtained using HFSS based on the finite element method (FEM). Theoretically, the scatterer has to satisfy $|J_{xx}| = |J_{yy}| = 1$ and $J_{xy} = J_{yx} = 0$, and also if J_{xx} and J_{yy} have a precise phase difference of 1 and π, then 100% PCR can be obtained [28]. The performance diagram is expressed by the polarization conversion parameters of the periodic unit cell when a rotation angle of $90°$ is considered as in Fig. 3. The results in Fig. 3(a) show that J_{xx} has band-pass characteristics, and J_{yy} has high-pass characteristics ($-J_{xx}| = |J_{yy}| = 0.94$ at 18.25 GHz). Also, $J_{xy} = J_{yx}$ is essentially equal to 0 ($\max|J_{xy}| = \max|J_{yx}| = 0.09$) due to the symmetry of the unit cell concerning the XZ-plane and YZ-plane mirrors. As shown in Fig. 3(b) at 18.25 GHz, exactly $\angle J_{xx}$-$\angle J_{yy} = \pi$, while a phase difference close to π is also obtained in 17–19 GHz. It is a valuable result that an absolute π phase difference can be obtained in the very high amplitude case. Fig. 4 shows the periodic cell of a CP wave incident on a parallel-stripe double-arrow structure to obtain the transmission coefficient magnitude and phase of the cross-polarized transmitted wave. Due to the symmetry of the periodic cell about the XZ and YZ planes, the cell rotation angle φ_r is set between $0°$ and $90°$ (angular step of $15°$). Fig. 4(a) indicates that the magnitude of the transmission coefficient is close to 0 dB with a
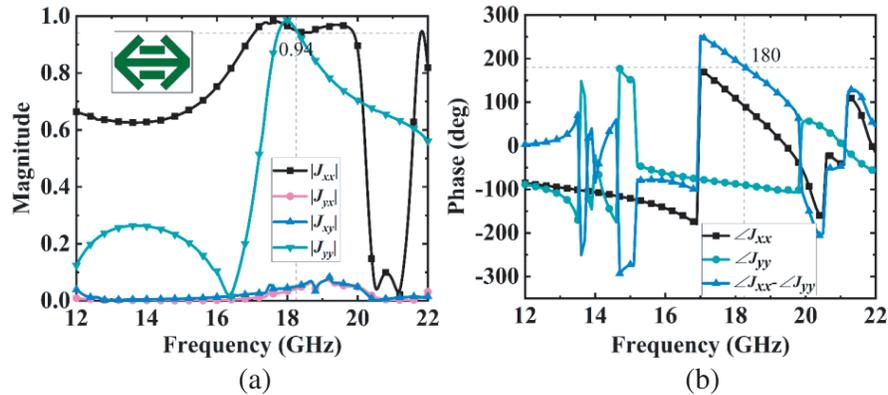

Figure 3. Schematic diagram of the periodic unit cell that achieves CP wave polarization conversion when the rotation angle is $90°$. (a) Magnitude. (b) Phase.
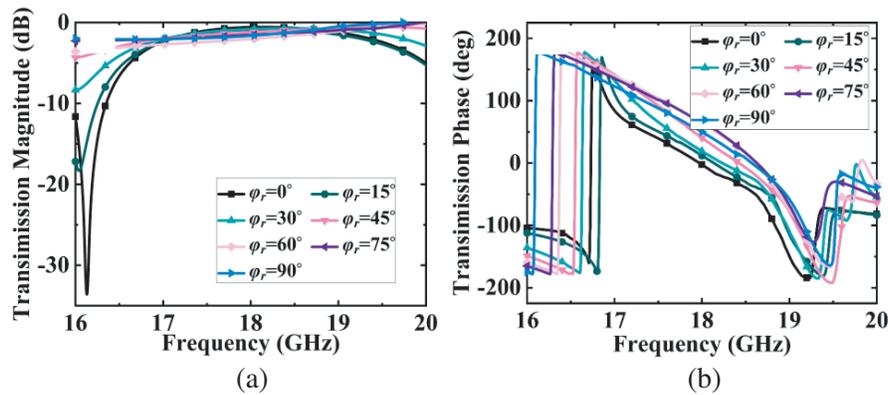
Figure 4. Transmission coefficient at different φ_r in 16–20 GHz. (a) Transmission magnitude. (b) Transmission phase.
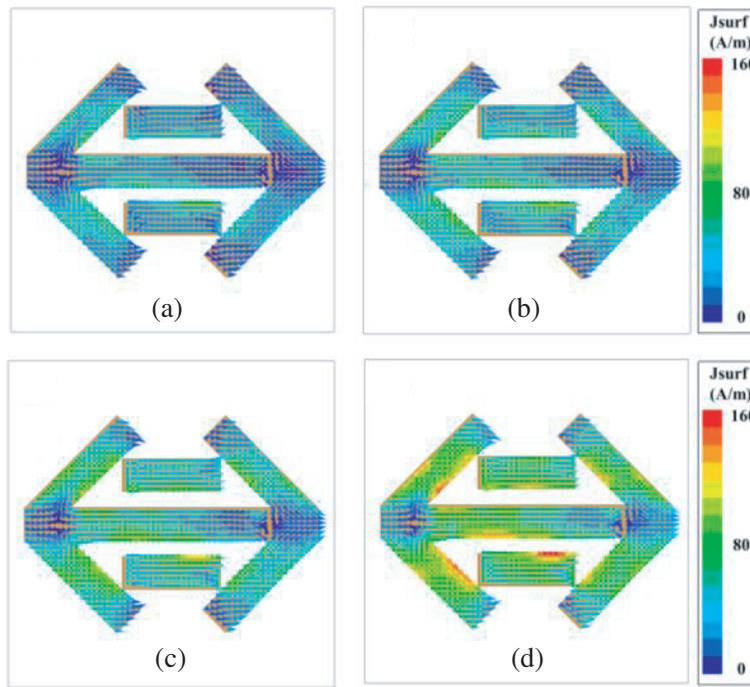

Figure 5. Surface current distribution of different LHCP incident waves radiating layers at 18 GHz with a rotation angle of 90°. (a) First layer. (b) Second layer. (c) Third layer. (d) Fourth layer.

maximum loss of 2.92 dB for different rotation angles φ_r in the band of 17–19 GHz. Any φ_r taken in the transmission phase of Fig. 4(b) yields a phase shift of 2π, with guaranteed transmission magnitude. The rotation angles are different, but they all can provide a linear variation. The linear phase shift obtained benefits from the modulation characteristics of the P-B phase, which is independent of frequency and only dependent on the rotation angle. The phase shift ranges from $-132.4°$ to $185.1°$ at a rotation angle of 75°. The reduction of the phase shift is due to the continuous oscillation of the transmission field between the metal layers of the multilayer structure at a specific angle. The LHCP wave is incident on different radiating layers at 18 GHz when the rotation angle is kept at 90° to illustrate and verify the polarization conversion performance. The surface current distributions of different radiating layers are demonstrated in Fig. 5. Figs. 5(a) to (d) show the surface currents of LHCP waves passing through the first to the fourth layer, respectively. The RHCP radiation characteristics are gradually revealed as

the number of radiating layers increases, and the dominant current vector direction is counterclockwise. This proves that the multilayer periodic unit cell achieves the polarization conversion of CP waves.

3. TMS DESIGN & PERFORMANCE ANALYSIS

3.1. TMS Design

The circularly polarized horn antenna located at the left center axis of the TMS serves as the feed antenna, in Fig. 6. The spherical wave generated by the feed source is incident on the TMS along the $+z$ direction to obtain the vortex wave. Metasurface with square aperture consists of 20×20 elements, assuming that the position of the periodic element on the TMS is (x_i, y_j), and the position of the feed antenna is (x_f, y_f, z_f). It can be deduced as follows:

$$\phi_{unit} = l \cdot \arctan\left(\frac{y_j}{x_i}\right) - k_0 \left[\sqrt{(x_i - x_f)^2 + (y_j - y_f)^2 + z_f^2} - z_f\right] \tag{7}$$

where l and k_0 are the expected OAM mode and free space propagation constant. The first term in Eq. (7) is the OAM wave, so the transmitted wave carries the desired mode. The second term is phase compensation, which makes up for the phase difference caused by the wave range difference. The phase required for the periodic cell is obtained by subtracting the OAM vortex term from the phase compensation term according to Eq. (7). Fig. 7 shows the MATLAB numerical solution simulation results at 18 GHz. The numerical solution can be seen to calculate the results with excellent OAM characteristics and high directionality of the transmitted wave phase distribution when l is taken as 2.
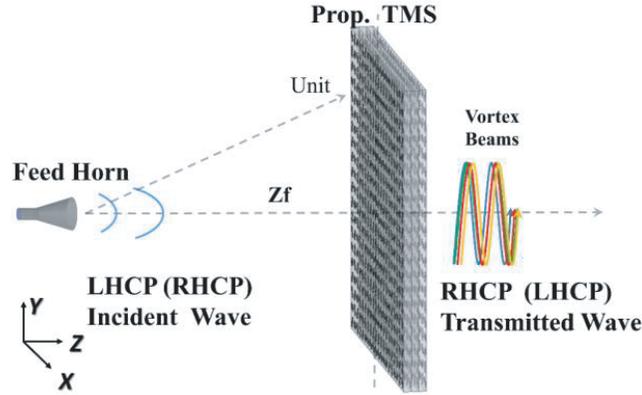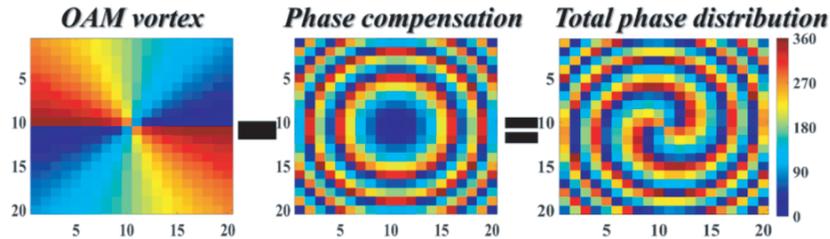

Figure 6. Schematic of TMS and feed horn.

Figure 7. Numerical solution of 20×20 TMS phase distribution with $l = 2$ at 18 GHz.

3.2. TMS Performance Analysis

The 20×20 square aperture TMS (size of $160 \times 160 \times 2.3\,\mathrm{mm}^3$) is constructed and simulated based on the periodic unit cell design and numerical analysis. The simulation results of the transmission
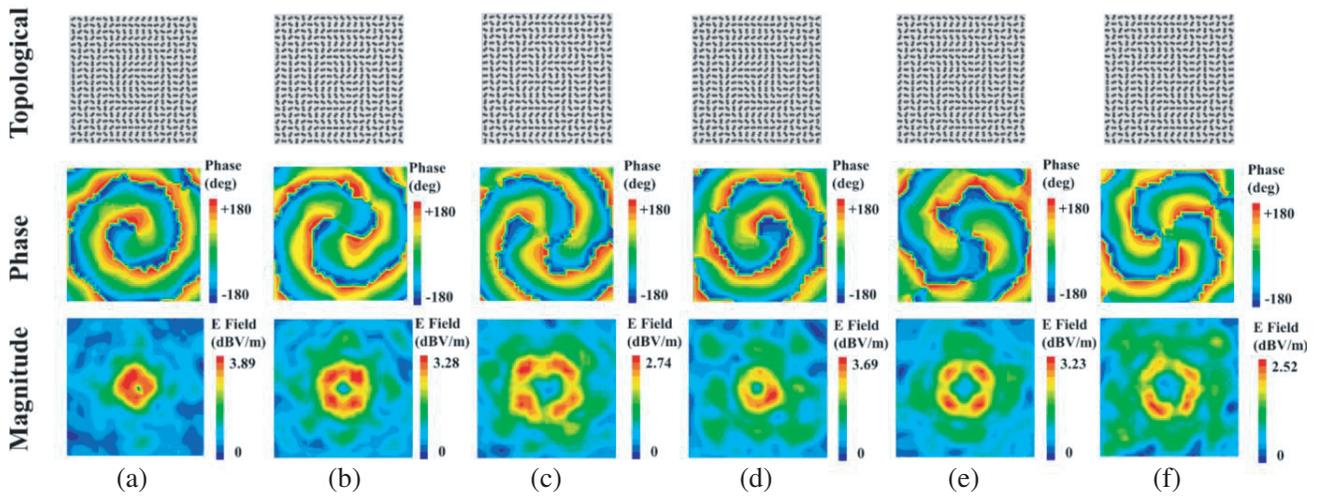
Figure 8. Simulation results of transmission magnitude and phase distribution observed under the proposed different planar topologies at 18 GHz. (a) and (d) mode ± 1, (b) and (e) mode ± 2, (c) and (f) mode ± 3.

phase and magnitude at 18 GHz for the OAM modes ± 1, ± 2, and ± 3, with the 2D topography of the respective mode TMSs, are presented in Fig. 8. The transmission magnitude shows the transmission E-field in different modes. The magnitude shows classical OAM characteristics; the center is a doughnut-like pattern with null. Meanwhile, the null point is deepened and increased with OAM modes. The transmission phase diagram shows that all-phase coverage of 2π can be achieved at modes ± 1, ± 2, and ± 3. The phase distribution demonstrates a spiral characteristic of 2π, 4π, and 6π counterclockwise rotation along the center when l is ± 1, ± 2, and ± 3, respectively. In individual phase diagrams, phase distortion disorder is at the edge of the reference plane due to the truncation effect caused by breaking the ideal periodicity of periodic unit cells in the X and Y directions under the actual array design. The proposed TMS unit cell structure can generate vortex waves from the magnitude and phase of transmission with ± 1, ± 2, and ± 3 modes.

Figure 9 constructs and demonstrates the test conditions of the TMS sample. The proposed $l = 2$ 20×20 square TMS in Fig. 9(a) shows a planar area of $200 \times 200\,\text{mm}^2$, whose effective radiating area is $160 \times 160\,\text{mm}^2$, manufactured and assembled using a general PCB technique. The modeling and numerical simulation processes already consider the effects of nylon columns and pressed laminates. A near-field anechoic chamber measures TMS at 120 mm from the feed horn in Fig. 9(b). Specifically, the LHCP quasi-Gaussian beam in the Ku-band excites the MS to avoid the truncation effect mentioned
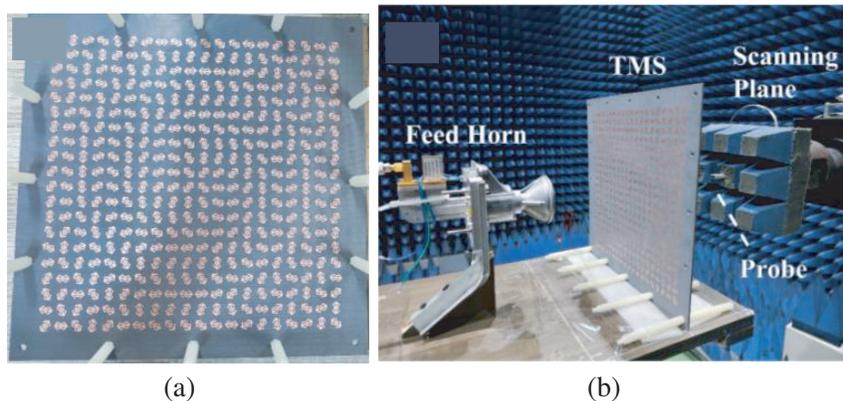

Figure 9. (a) 20×20 TMS with $l = 2$. (b) Near-field measurement.
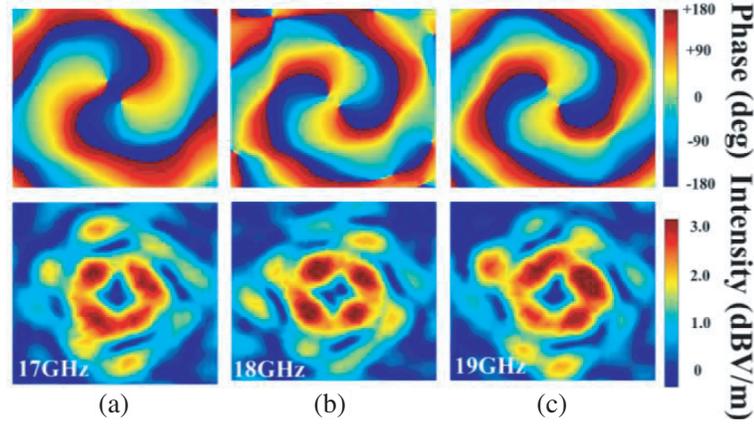
Figure 10. The transmission magnitude and phase of the square aperture TMS with $l = 2$ at different frequencies were measured. (a) 17 GHz. (b) 18 GHz. (c) 19 GHz.

above. Also, the reference plane where the standard waveguide probe is located is 200 mm away from the MS, created on the other side. The reference scanning plane is set to $420 \times 420 \, \text{mm}^2$, and the scanning step is set to 2 mm. Fig. 10 presents the results of the measured transmission intensity and phase distribution. It is observed from the measured results that the center is the null-magnitude region of the E-field intensity of the RHCP wave. The phase peak front variations at 17 GHz, 18 GHz, and 19 GHz all satisfy 2π. Typical +2 mode OAM waves are corroborated.

Furthermore, we discuss the purity of the proposed OAM model for TMS. The toroidal E-field around the null-magnitude point is taken separately in the transmission magnitude field in Fig. 10 for Fourier transform analysis [29]:

$$A_l = \frac{1}{2\pi} \int_0^{2\pi} \psi(\varphi) d\varphi e^{-jl\varphi} \tag{8}$$

$$\psi(\varphi) = \sum_l A_l e^{jl\varphi} \tag{9}$$

where $\psi(\varphi)$ is a function of the sampling field, and A_l is the magnitude of the corresponding mode. The ratio of each modal component to the total energy can express the purity of OAM. Fig. 11 shows the purity energy weights of OAM mode 2 in the proposed band, 78.8% of the simulated purity at 17 GHz (72.7% measured), 79.4% of the simulated purity at 18 GHz (73.5% measured), and 78.5% of the simulated purity at 19 GHz (70.8% measured). The primary mode energy is much larger than the other modes, and the inter-mode interference can be neglected.
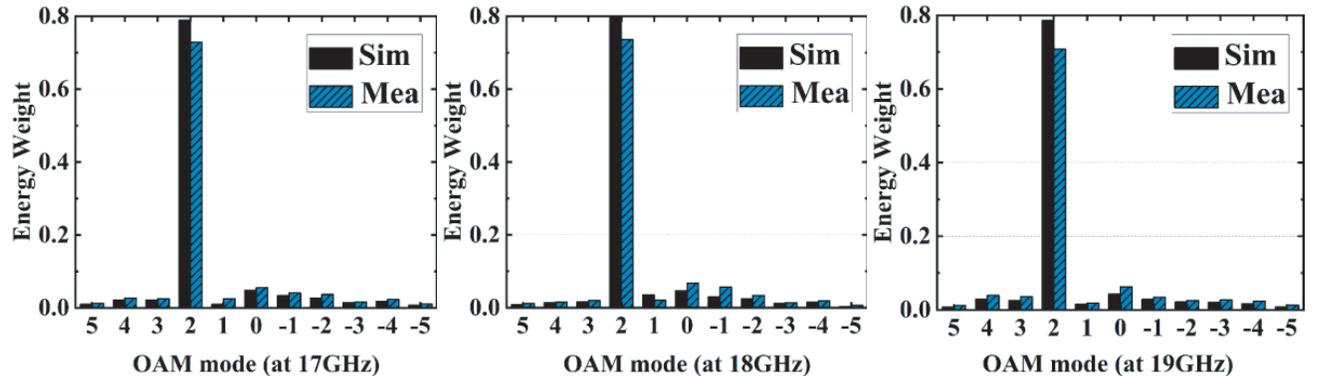

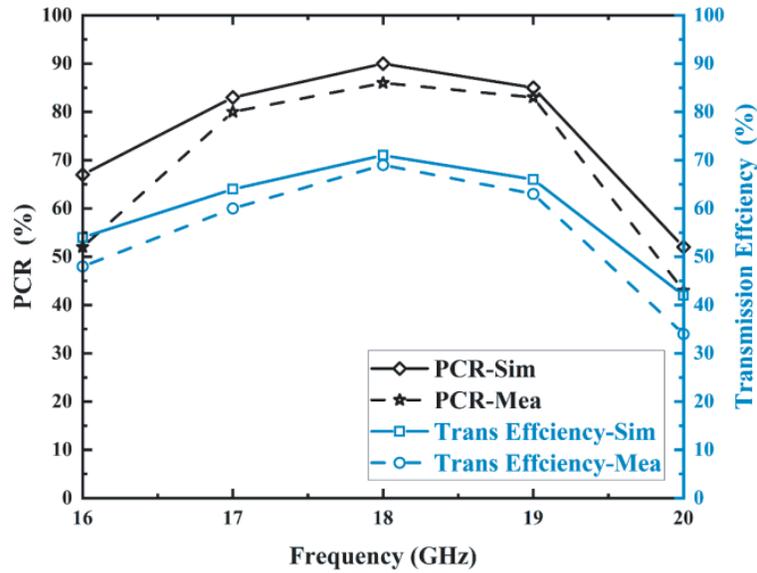**Figure 11.** Purity of OAM mode at different frequencies.

Figure 12. Transmission efficiency and PCR of TMS with $l = 2$.

The TMS' PCR and transmission efficiency were measured and analyzed. PCR is the ratio of cross-polarized vortex wave energy to the total transmitted wave, and transmission efficiency is the ratio of transmitted wave energy to the incident wave. Fig. 12 shows the simulated and measured results of PCR and transmission efficiency. At 17–19 GHz, the simulated data of PCR are 83.2–90.1% (measured 80.1–86.3%), and the simulated data of transmission efficiency are 63.7–70.8% (measured 59.7–69.3%). The proposed passband's average PCR and transmission efficiency values are 83.3% and 64.4%, respectively. These are attributed to the excellent transmission efficiency and precise π-phase difference of the periodic unit cell, and on the other hand, to the vast radiation aperture of the TMS. Unfortunately, the PCR has difficulty achieving theoretical results when metal losses, dielectric losses, and reflections at the air-dielectric interface are considered.

To illustrate the advantages of this scheme, the designed TMS is compared with the proposed OAM planar antenna in Table 2. Since the MS has the advantages of compact structure, simple feeding, and low cost compared with other OAM non-planar antennas, the comparison is not made here. The proposed TMS's advantage combines high conversion efficiency (83.3%) and high transmission efficiency (64.4%) with broadband, high purity, and miniaturization. Although the transmission efficiency of [30, 31] is higher than the present design, [31, 32] use a transmission phase design with a strong chromatic response leading to a narrow operating band, and the conversion efficiency of [31] is unknown. Meanwhile, [30] has a large bandwidth and high transmission efficiency, but the measured OAM purity is limited. Using an all-dielectric meta-lens platform with a barbell-type periodic cell profile height of $2.2\lambda_0$ causes the problem of large antennas. Ref. [33] obtains multiple OAM transmissive waves in ± 1, ± 2, ± 3, ± 4 modes by using controlled PIN on/off. However, the periodic unit cell uses a 13-layer PIN reconfigurable design with a phase-modulated structure with a profile height of $2.6\lambda_0$. Refs. [22, 34] use the Pancharatnam-Berry phase principal design, and both obtain high conversion efficiency. Unfortunately, it is also impossible to obtain a high transmission efficiency. Ref. [25] shows high PCR and transmission efficiency in X-band, but has the dilemma of too large aperture area. The numerical simulation results are in high consistencies, with the measured results showing that the demonstrated TMS can generate high-purity vortex waves stably and efficiently considering broadband and high efficiency. This vortex wave can prevent beam shift and misalignment and utilize the advantages of OAM waves well, which are applied to achieve OAM multiplexing and fast alignment in the Ku-band.

Table 2. Performance comparison of the designed TMS with the present OAM planar antenna.

Ref.	Antenna Type (Polarization)	Frequency Bands (GHz)	Aperture Size (λ)	OAM modes	Periodic Unit Cell		PCR (%)	Efficiency (%)	OAM Purity (%)
					Transmission Loss (dB) or Transmittance (%)	Phase Shift (deg)			
[30]	Meta-lens (LP)	26.5–40.0 (40.6%)	$12.2 \times 12.2 \times 2.2$	1	$> 68\%$	360		59.5–86.2	> 50.0
[31]	ME-FSS (LP)	10.6	$8.5 \times 8.5 \times 0.2$	1	$> 90\%$	360		> 60.0	
[32]	TAs (LP)	10.0	$8.0 \times 8.0 \times 0.2$	1	$< 0.5\,\mathrm{dB}$	360		11.9	> 81.5
[33]	PIN Reconfigurable (-)	10.0	$6.9 \times 7.3 \times 2.6$	± 1 & ± 2 & ± 3 & ± 4	$< 0.3\,\mathrm{dB}$	> 360			> 60 & > 60 & 50 & 40
[34]	FSS (CP)	10.0–11.1 (10.4%)	$12.5 \times 12.5 \times 0.1$	2	$> 80\%$	~ 360	Near 100% (10.7 GHz)	> 50.0	93.4
[22]	TMS (CP)	10.0	$6.0 \times 6.0 \times 0.1$	1 2	90%	360	75.0 71.0	54.0 39.0	
[25]	TMS (CP)	7.5–10.5 (33.3%)	Circle with diameter 12λ	2	$> 80\%$	360	80.0	60.0	
Prop.	TMS (CP)	17–19 (11.1%)	$9.6 \times 9.6 \times 0.1$	± 1 & ± 2 & ± 3	0.2–2.9 dB	~ 360	83.3	64.4	> 70.8

λ_0: Free space wavelength at the center frequency.

4. CONCLUSION

This paper presents a TMS based on a multilayer parallel-stripe double-arrow periodic cell composition to realize broadband polarization-converted vortex waves in different OAM modes in Ku-band. We theoretically analyze the transmission properties of the proposed anisotropic scatterer by introducing the Jones matrix. Meanwhile, the periodic unit cell has a phase shift greater than 2π and a transmission loss less than 2.92 dB in the range of 17–19 GHz. Further, the TAs with $l = \pm 1$, ± 2, and ± 3 designed using the P-B phase principle achieve full phase control. The manufactured $l = 2$ TMS can convert the LHCP incident wave into RHCP vortex wave in the working frequency band (17–19 GHz), with PCR and transmission efficiency of 83.3% and 64.4%, respectively. The design can efficiently generate polarization-inverted OAM waves while considering broadband and high purity. Broadband high-efficiency vortex waves in TAs are of great constructional importance to check beam shift for assisting UAVs and satellite alignment.

REFERENCES

1. Edfors, O. and A. J. Johansson, "Is Orbital Angular Momentum (OAM) based radio communication an unexploited area?" *IEEE Transactions on Antennas and Propagation*, Vol. 60, No. 2, 1126–1131, Feb. 2012.
2. Morabito, A. F., L. Di Donato, and T. Isernia, "Orbital angular momentum antennas," *IEEE Antennas and Propagation Magazine*, Vol. 60, No. 2, 59–67, Apr. 2018.
3. Liu, K., X. Li, Y. Gao, H. Wang, and Y. Cheng, "Microwave imaging of spinning object using orbital angular momentum," *Journal of Applied Physics*, Vol. 122, No. 12, Art. No. 124903, Sep. 28, 2017.

4. Wang, J., K. Liu, Y. Cheng, and H. Wang, "Vortex SAR imaging method based on OAM beams design," *IEEE Sensors Journal*, Vol. 19, No. 24, 11873–11879, Dec. 15, 2019.

5. Barbuto, M., A. Alu, F. Bilotti, and A. Toscano, "Dual-circularly polarized topological patch antenna with pattern diversity," *IEEE Access*, Vol. 9, 48769–48776, 2021.

6. Andersen, J. M. S. N. Alperin, A. A. Voitiv, W. G. Holtzmann, J. T. Gopinath, and M. E. Siemens, "Characterizing vortex beams from a spatial is light modulator with collinear phase-shifting holography," *Applied Optics*, Vol. 58, No. 2, 404–409, Jan. 10, 2019.

7. Tamagnone, M. C. Craeye, and J. Perruisseau-Carrier, "Encoding many channels on the same frequency through radio vorticity: First experimental test," *New Journal of Physics*, Vol. 14, No. 11, 2012.

8. Kaniewski, P., W. Komorniczak, C. Leśnik, et al., "S-band and Ku-band SAR system development for UAV-based applications," *Metrology and Measurement Systems*, Vol. 26, No. 1, 53–64, 2019.

9. Lv, Z. X., X. L. Qiu, Y. Cheng, S. T. Shangguan, F. F. Li, and C. B. Ding, "Multi-rotor UAV-borne PolInSAR data processing and preliminary analysis of height inversion in urban area," *Remote Sensing*, Vol. 14, No. 9, Art. No. 2161, May 2022.

10. Iqbal, M. N., M. F. M. Yusoff, M. K. A. Rahim, M. R. Hamid, Z. Johari, and H. U. Rahman, "A high gain and compact transmitarray antenna for Ku-band satellite communications," *Electromagnetics*, Vol. 41, No. 5, 331–343, Jul. 4, 2021.

11. Abdulkarim, Y. I., L. Deng, H. N. Awl, et al., "Design of a broadband coplanar waveguide-fed antenna incorporating organic solar cells with 100% insolation for Ku band satellite communication," *Materials (Basel)*, Vol. 13, No. 1, Art. No. 142, Dec. 30, 2019.

12. Isakov, D., Y. Wu, B. Allen, P. S. Grant, C. J. Stevens, and G. J. Gibbons, "Evaluation of the Laguerre-Gaussian mode purity produced by three-dimensional-printed microwave spiral phase plates," *Royal Society Open Science*, Vol. 7, No. 7, Art. No. 200493, Jul. 22, 2020.

13. Zhang, Y.-M. and J.-L. Li, "An orbital angular momentum-based array for in-band full-duplex communications," *IEEE Antennas and Wireless Propagation Letters*, Vol. 18, No. 3, 417–421, Mar. 2019.

14. Xin, M., R. Xie, G. Zhai, et al., "Full control of dual-band vortex beams using a high-efficiency single-layer bi-spectral 2-bit coding metasurface," *Optics Express*, Vol. 28, No. 12, 17374–17383, Jun. 8, 2020.

15. Qin, F., S. Gao, W.-C. Cheng, Y. Liu, H.-L. Zhang, and G. Wei, "A high-gain transmitarray for generating dual-mode OAM beams," *IEEE Access*, Vol. 6, 61006–61013, 2018.

16. Iqbal, S., S. Liu, J. Luo, L. Zhang, H. A. Madni, and T. J. Cui, "Controls of transmitted electromagnetic waves for diverse functionalities using polarization-selective dual-band 2bit coding metasurface," *Journal of Optics*, Vol. 22, No. 1, Art. No. 015104, Jan. 2020.

17. Iqbal, S., J. Luo, Q. Ma, et al., "Power modulation of vortex beams using phase/amplitude adjustable transmissive coding metasurfaces," *Journal of Physics D — Applied Physics*, Vol. 54, No. 3, Art. No. 035305, Jan. 21, 2021.

18. Shahmirzadi, A. V., Z. Badamchi, B. Badamchi, and H. Subbaraman, "Generating concentrically embedded spatially divided OAM carrying vortex beams using transmitarrays," *IEEE Transactions on Antennas and Propagation*, Vol. 69, No. 12, 8436–8448, 2021.

19. Shahmirzadi, A. V. and A. A. Kishk, "OAM carrying vortex beam mode interconversion using modular cascaded transmitarrays," *IEEE Transactions on Microwave Theory and Techniques*, Vol. 70, No. 7, 3591–3605, 2022.

20. Lv, H. H., Q. L. Huang, X. J. Yi, J. Q. Hou, and X. W. Shi, "Low-profile transmitting metasurface using single dielectric substrate for OAM generation," *IEEE Antennas and Wireless Propagation Letters*, Vol. 19, No. 5, 881–885, May 2020 (in English).

21. Bai, X. D., "High-efficiency transmissive metasurface for dual-polarized dual-mode OAM generation," *Results in Physics*, Vol. 18, Sep. 2020.

22. Akram, M. R., X. Bai, R. Jin, G. A. E. Vandenbosch, M. Premaratne, and W. Zhu, "Photon spin hall effect-based ultra-thin transmissive metasurface for efficient generation of OAM waves," *IEEE Transactions on Antennas and Propagation*, Vol. 67, No. 7, 4650–4658, 2019.

23. Arbabi, A. and A. Faraon, "Fundamental limits of ultrathin metasurfaces," *Scientific Reports*, Vol. 7, 43722, Mar. 6, 2017.

24. Zhang, K., Y. Yuan, D. Zhang, et al., "Phase-engineered metalenses to generate converging and non-diffractive vortex beam carrying orbital angular momentum in microwave region," *Opt Express*, Vol. 26, No. 2, 1351–1360, Jan. 22, 2018.

25. Jiang, S., C. Chen, H. Zhang, and W. Chen, "Achromatic electromagnetic metasurface for generating a vortex wave with Orbital Angular Momentum (OAM)," *Opt Express*, Vol. 26, No. 5, 6466–6477, Mar. 5, 2018.

26. Bouchard, F., I. De Leon, S. A. Schulz, J. Upham, E. Karimi, and R. W. Boyd, "Optical spin-to-orbital angular momentum conversion in ultra-thin metasurfaces with arbitrary topological charges," *Applied Physics Letters*, Vol. 105, No. 10, Art. No. 101905, Sep. 8, 2014.

27. Chen, M. L. N., L. J. Jiang, and W. E. I. Sha, "Artificial perfect electric conductor-perfect magnetic conductor anisotropic metasurface for generating orbital angular momentum of microwave with nearly perfect conversion efficiency," *Journal of Applied Physics*, Vol. 119, No. 6, 2016.

28. Chen, M. L. N., L. J. Jiang, and W. E. I. Sha, "Ultrathin complementary metasurface for orbital angular momentum generation at microwave frequencies," *IEEE Transactions on Antennas and Propagation*, Vol. 65, No. 1, 396–400, 2017.

29. Jack, B., M. J. Padgett, and S. Franke-Arnold, "Angular diffraction," *New Journal of Physics*, Vol. 10, No. 10, 2008.

30. Lin, M., J. Yi, J. Wang, et al., "Single-layer re-organizable all-dielectric meta-lens platform for arbitrary transmissive phase manipulation at millimeter-wave frequencies," *IEEE Transactions on Antennas and Propagation*, Vol. 70, No. 3, 2059–2069, Mar. 2022.

31. Wang, Y., K. Zhang, Y. Yuan, et al., "Generation of high-efficiency vortex beam carrying OAM mode based on miniaturized element frequency selective surfaces," *IEEE Transactions on Magnetics*, Vol. 55, No. 10, 1–4, 2019.

32. Qin, F., R. Song, W. Cheng, and H. Zhang, "Multibeam OAM transmitarray with stable vortex property based on bifocal method," *IEEE Antennas and Wireless Propagation Letters*, Vol. 20, No. 9, 1601–1605, Sep. 2021.

33. Wang, X., Y. Chen, S. Zheng, and X. Zhang, "Reconfigurable OAM antenna based on sub-wavelength phase modulation structure," *IET Microwaves Antennas & Propagation*, Vol. 12, No. 3, 354–359, Feb. 28, 2018.

34. Wang, Y., K. Zhang, Y. Yuan, et al., "Planar vortex beam generator for circularly polarized incidence based on FSS," *IEEE Transactions on Antennas and Propagation*, Vol. 68, No. 3, 1514–1522, Mar. 2020.